The Influence of Large-Scale Spatial Warming on Jet Stream Extreme Waviness on an Aquaplanet

Thomas J. Batelaan[1], Chris Weijenborg[1], Gert-Jan Steeneveld[1], Chiel C. van Heerwaarden[1], and Victoria Anne Sinclair[2]

[1]Wageningen University
[2]University of Helsinki

April 16, 2024

Abstract

The effect of modified equator-to-pole temperature gradients on the jet stream by low-level polar warming and upper-level tropical warming on jet streams is not fully understood. We perform four aquaplanet simulations to quantify the impact of different sea surface temperature distributions on jet stream strength, wave amplitudes and jet stream waviness, quantified by a modified Sinuosity Index. A large-scale uniform warming scenario increases the jet strength whereas decreases in jet strength occur in two scenarios where the meridional temperature gradient is reduced. However, all scenarios indicate substantial decreases in the magnitude of large wave amplitudes, jet stream extreme waviness and reduced variability of these diagnostics, suggesting a relationship with weakened baroclinicity. Our findings contradict the earlier proposed mechanism that low-level polar warming weakens the jet stream and increases wave amplitudes and jet stream waviness. We conclude that a weaker jet stream does not necessarily become wavier.

The Influence of Large-Scale Spatial Warming on Jet Stream Extreme Waviness on an Aquaplanet

T. J. Batelaan[1], C. Weijenborg[1], G.J. Steeneveld[1], C. C. van Heerwaarden[1], V. A. Sinclair[2]

[1]Meteorology and Air Quality Section, Environmental Sciences Group, Wageningen University, P.O. Box 47, 6700 AA Wageningen, The Netherlands
[2]Institute for Atmospheric and Earth System Research/Physics, Faculty of Science, University of Helsinki, P.O. Box 64, 00014, Helsinki, Finland

Key Points:

- Weakened jet streams do not become wavier on an aquaplanet with reduced temperature gradients due to warming in mid- and high latitudes
- The magnitude of large wave amplitudes and jet stream extreme waviness decrease robustly under large-scale spatial warming on an aquaplanet

Corresponding author: Thomas J. Batelaan, `thomas.batelaan@wur.nl`

Abstract

The effect of modified equator-to-pole temperature gradients on the jet stream by low-level polar warming and upper-level tropical warming on jet streams is not fully understood. We perform four aquaplanet simulations to quantify the impact of different sea surface temperature distributions on jet stream strength, wave amplitudes and jet stream waviness, quantified by a modified Sinuosity Index. A large-scale uniform warming scenario increases the jet strength whereas decreases in jet strength occur in two scenarios where the meridional temperature gradient is reduced. However, all scenarios indicate substantial decreases in the magnitude of large wave amplitudes, jet stream extreme waviness and reduced variability of these diagnostics, suggesting a relationship with weakened baroclinicity. Our findings contradict the earlier proposed mechanism that low-level polar warming weakens the jet stream and increases wave amplitudes and jet stream waviness. We conclude that a weaker jet stream does not necessarily become wavier.

Plain Language Summary

This research letter considers how different patterns of atmospheric warming, like low-level warming at the poles and at high altitude in the tropics, impact the jet stream, which is a strong ‘river’ of high-altitude wind. We use numerical model simulations to mimic different scenarios of warming that maintain or reduce the temperature gradient between equator and poles. We find that when an Earth-like planet completely covered by water warms in specific ways, it strengthens or weakens the jet stream, but reduces the size of its largest waves, and makes the extreme waviness episodes less wavy. We explain that this is possibly related to the reduced energy available to grow weather systems. Furthermore, this research letter conclude that weakened jet streams do not necessarily become wavier, which is against the idea that weakened jet streams become wavier due to warming in polar regions.

1 Introduction

Key characteristics of anthropogenic global warming are polar amplification and upper tropospheric tropical warming (e.g., IPCC, 2021; Gulev et al., 2021; Lee et al., 2021; Doblas-Reyes et al., 2021). These large-scale spatial warming phenomena alter the equator-to-pole temperature gradient in the lower and upper troposphere, which, in turn, initiates the "meridional tug-of-war on the jet stream" (Barnes & Screen, 2015; Shaw et al., 2016; Stendel et al., 2021).

The impact of the altered meridional temperature gradients on the jet stream remains a subject of ongoing research (e.g., Coumou et al., 2018; Vavrus, 2018; Cohen et al., 2020). Recently, Woollings et al. (2023) found that the observed weak poleward jet shift could be potentially linked to upper tropospheric tropical warming. However, most studies focus on the influence of amplified Arctic warming on the jet stream and several hypotheses have been put forward (see e.g., Cross-Chapter Box 10.1 Doblas-Reyes et al., 2021). For instance, Francis and Vavrus (2012, 2015) hypothesized that a weaker jet stream, caused by polar amplification, would become more wavy, potentially leading to more frequent weather extremes. This hypothesis is that a wavy jet stream is associated with atmospheric blocking and Rossby wave breaking, which are known to be related to mid-latitude weather extremes (Woollings et al., 2018). While this hypothesis has generated much discussion over the past decade, it has yet to be conclusively confirmed or refuted (e.g., Barnes, 2013; Barnes & Screen, 2015; Cohen et al., 2020).

Most studies about projected waviness changes with comprehensive climate models indicate a decrease in waviness (Barnes & Polvani, 2015; Cattiaux et al., 2016; Peings et al., 2017) but with a large intermodel spread. To disentangle processes in highly nonlinear climate models, numerous studies have attempted to replicate Arctic amplification through prescribed sea-ice loss in climate models and test the influence on circulation (Screen et al., 2018; Smith et al., 2019). However, the findings of these studies are still inconclusive, confirming the link (Mori et al., 2019), noting no clear differences in waviness (e.g., Ogawa et al., 2018; Blackport & Screen, 2020) or showing weak responses to sea-ice loss (Smith et al., 2022). To even further reduce complexity in the search of causality, highly idealized modeling studies have investigated the impact of changes in the meridional temperature gradient alone. However, they have focused on migration of the storm track (Butler et al., 2010), on the effect of blocking (Hassanzadeh et al., 2014) and temperature variability (Schneider et al., 2015) rather than on waviness changes. Schemm and Röthlisberger (2024) do study jet stream waviness changes, however only under uniform warming.

This research letter focuses on changes of jet stream extreme waviness, associated with large amplitude waves and weather extremes, in an highly idealized model framework. We have conducted four simulations with the OpenIFS model in aquaplanet configuration in which we have increased the Sea Surface Temperatures (SSTs) while either maintaining or reducing the meridional gradients. Compared to previous highly idealized studies (Butler et al., 2010; Hassanzadeh et al., 2014) we retained moist processes that can yield significant feedback on the dynamics (Vallis, 2020). Moreover, a more realistic mean temperature distribution and meridional temperature gradient reductions are established compared to previous studies (Hassanzadeh et al., 2014; Schneider et al., 2015).

Conducting these simulations, we aim to determine the influence of large-scale spatial warming on jet stream extreme waviness. We first discuss the modeled influence of the altered SSTs on the zonal mean temperature distribution and the atmospheric jet. Thereafter we discuss if the changed mean state possibly leads to changes in the largest amplitudes of the waves in the jet stream, jet stream extreme waviness and cut-off segments related to blocking highs and cut-off lows that are associated with weather extremes (Cattiaux et al., 2016).

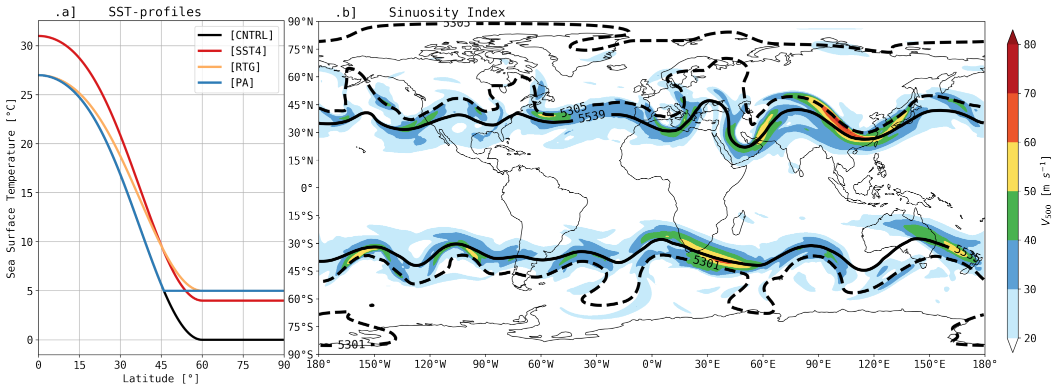

Figure 1. a] Prescribed SST [°C] profiles as a function of latitude for the four model experiments. The profiles are zonally uniform and symmetric about the equator. b] Sinuosity Index [-] visualized for a selected timestep of the [CNTRL]-simulation. The black dashed contour line is the average $Z500$ isohypse [m] based on the original SI metric and the black solid contour line is the average $Z500$ isohypse based on our modified SI method. Shading denotes the 500-hPa wind speed [m s^{-1}]. Coastlines are included for reference, but are nonexistent in the simulations.

2 Methods

2.1 OpenIFS

We use the numerical weather prediction model OpenIFS, developed by the European Center for Medium Range Weather Forecasts (ECMWF). OpenIFS shares the same dynamical core and physical parametrizations as the Integrated Forecast System (IFS) which is used for operational weather forecasting at ECMWF. However, compared to IFS, OpenIFS lacks data assimilation capacity and is not coupled to an ocean model. We use version Cy43r3v2 that was operational between July 2017 and June 2018 (documentation online at `https://www.ecmwf.int/en/publications/ifs-documentation`).

2.2 Experimental Setup

The experimental setup and initial conditions follow Sinclair and Catto (2023). The simulations run in the aquaplanet configuration with fixed zonally uniform SSTs. The incoming solar radiation is specified at the equinoctial value to remove seasonal variation, but a diurnal cycle is present. The simulations run at T255 resolution (grid spacing of about 78 km at the equator) and with 60 vertical model levels with the model top at 0.1 hPa. The initial conditions are modified from a randomly selected real atmospheric state from the ERA5-reanalysis (Hersbach et al., 2020). First, the land–sea mask is changed to cover the whole globe by ocean. Second, the surface geopotential is set to zero everywhere. Finally, the atmospheric fields are interpolated to the new flat surface in regions where there is topography on Earth.

We conduct four experiments, i.e. [CNTRL], [SST4], and [PA] following Sinclair and Catto (2023) and an additional Reduced Temperature Gradient [RTG] simulation. The simulations are selected because compared to [CNTRL] they establish large-scale spatial warming with upper tropical warming in [SST4], polar amplification in [PA] and gradual warming from the equator resulting in a large meridional temperature gradient reduction in [RTG]. Through executing these four simulations we are able to study the impact of large-scale spatial warming on jet stream waviness.

The control simulation [CNTRL] follows the SST-profile QObs of Neale and Hoskins (2000) that tries to resemble Earth's SSTs. It has maximum SSTs of 27°C on the equator decreasing poleward to 0°C at 60° latitude from where they remain constant (Figure 1a). The [SST4] simulation has a uniform warming of 4°C compared to the [CNTRL] simulation (Figure 1a). This results in upper tropical warming (Sinclair et al., 2020; Sinclair & Catto, 2023). The polar amplification simulation [PA] (AA in Sinclair & Catto, 2023) uses the QObs SST distribution between 45°S and 45°N, with SSTs set to 5°C poleward of these latitudes to mimic polar amplification (Figure 1a). Compared to [CNTRL] the SSTs of the [RTG] simulation are gradually warmed from the equator with the maximum temperature increase of 5°C occurring poleward of 60° latitude (Figure 1a). This additional simulation is conducted to simulate a more realistic equator-to-pole temperature gradient reduction, with warming occurring in the subtropics, mid-latitudes, and polar regions, rather than just at high latitudes as in the [PA] simulation.

Each simulation is run for a total of 11 years. This simulation length is long enough to capture internal variability as there is no seasonal cycle in our simulations. However, to ensure a balanced state is achieved, the first year of each simulation is discarded. Model output is saved every six hours on 22 pressure levels between 1000 hPa and 10 hPa.

2.3 Jet Stream Waviness Quantification

To quantify waviness different methods exist (e.g. Francis & Vavrus, 2012; Chen et al., 2015; Cattiaux et al., 2016; Di Capua & Coumou, 2016; Röthlisberger, Martius, & Wernli, 2016; Martin, 2021). Dynamical approaches use concepts based on energy conservation while geometric approaches aim to capture the shape of the waves (Vavrus, 2018). We use the geometric *Sinuosity Index* (SI) by Cattiaux et al. (2016) because their method includes cut-off segments related to blocking highs and cut-off lows and has been used in conjunction with the Local Wave Activity metric (Chen et al., 2015) without divergent outcomes (Blackport & Screen, 2020). Moreover, the SI method is defined at the 500 hPa pressure level that has the advantage to be insensitive to heating (Barnes, 2013; Cattiaux et al., 2016). SI is computed every 6 hours to capture synoptic-scale variability.

Cattiaux et al. (2016) compute the SI as a measure of the mean flow around 50° latitude. First they calculate the average 500-hPa geopotential height, $Z500$, between 30° and 70° latitude. Then, Cattiaux et al. (2016) define the SI as the ratio between the length of the isohypse with the estimated $Z500$ value to the circumference of the Earth at 50° latitude.

Unfortunately, the original SI metric does not adequately capture the jet stream in the aquaplanet setup (Figure 1b). Specifically, the isohypse do not align well with the wind maxima associated with the jet stream and also contains segments at high latitudes that are unrelated to the jet stream or atmospheric blocks. To address this issue, we develop a new method to determine the latitudinal range $_{\Delta\phi}$ over which to calculate the $Z500$ average. Specifically, we identify $_{\Delta\phi}$ in each hemisphere where the time mean zonal mean magnitude of the horizontal wind vector at 500 hPa $[\overline{V_{500}}]$ exceeds half of its climatological maximum of $[\overline{V_{500}}]$ (Figure S1), where the overbar represents time mean and square brackets denoted the zonal mean. By using this method, we find the following latitude ranges per simulation per hemisphere: (21.4°N, 47.4°N) & (22.1°S, 47.4°S) for the [CNTRL]-simulation, (22.8°N, 51.6°N) & (22.1°S, 51.6°S) for the [SST4] simulation, (20.7°N, 49.5°N) & (21.4°S, 49.5°S) for the [RTG] simulation and (20.7°N, 45.3°N) & (21.3°S, 45.3°S) for [PA]. We find the same latitude ranges if we use the zonal mean zonal wind ($[\overline{u_{500}}]$) instead of $[\overline{V_{500}}]$. Between the above mentioned latitudinal ranges we calculate the average $Z500$ at every timestep which is then used as the selected value of the isohypse to calculate its length.

Moreover, Cattiaux et al. (2016) use a constant normalization of circumference of the Earth at 50° latitude, but to account for the latitudinal jet stream migration we normalize the length of the $Z500$ isohype with the circumference of the Earth at the mean latitude of the selected isohypse $\tilde{\phi}_{Z500}$. The resulting modified SI is defined as follows:

$$SI(\phi, t) = \frac{\text{arclength}(Z500_{\Delta\phi}(t))}{2\pi a \cos(\tilde{\phi}_{Z500}(\phi, t))}, \tag{1}$$

where $Z500_{\Delta\phi}$ is the average geopotential height at 500 hPa between the above mentioned latitudinal ranges per simulation per hemisphere $_{\Delta\phi}$, a denotes the radius of Earth and $\tilde{\phi}_{Z500}$ is the mean latitude of the selected $Z500$ isohypse. A value of SI=1 indicates a straight westerly atmospheric flow, whereas SI values in the range 2-3 indicate a strongly meandering flow with the average $Z500$ isohypse being 2-3 times longer than the circumference of the Earth at the mean latitude.

Further, we use the meridional extent defined as the difference between the maximum and minimum latitude of the selected $Z500$ isohypse, to quantify the wave amplitude (Barnes, 2013). Moreover, the SI metric enables the possibility to differentiate between the circumglobal isohypse and cut-off segments related to blocking highs and cut-off lows that are associated with weather extremes, as shown by Cattiaux et al. (2016). We only maintain cut-off segments that are larger than the circumference of a circle with radius of 78 km (i.e. 1 grid cell).

3 Mean State Response in Temperature (gradient) and Zonal Wind

All simulations display zonal mean climatologies of temperature and zonal wind that are generally consistent with observations of the Earth's atmosphere (Figure 2, row 1 and 3). The core of the jet streams are located near 30° latitude at tropopause level. The dynamical tropopause, defined as the 2 PVU-surface, has physically plausible values that vary between 100 hPa in the tropics and 300 hPa at the poles (Figure 2). The simulations exhibit almost perfect symmetry, as would be expected from the aquaplanet set up.

3.1 [SST4] simulation

The [SST4] simulation reveals the most substantial tropospheric warming of all simulations. Climatological temperature increases of over 5 K are ubiquitous (Figure 2a). The warming signal is particularly strong in the upper tropical troposphere, exceeding 10 K due to enhanced latent heat release in the rising branch of the Hadley cells (not shown). The tropospheric warming leads to a deeper troposphere, as indicated by the lifted dynamic tropopause (Figure 2, column 1). Furthermore, the lower polar stratosphere cools, which is potentially due to a weakened Brewer-Dobson circulation.

The combined impact of the deeper troposphere, upper tropospheric tropical warming and lower stratospheric polar cooling in the [SST4] simulation results in an enhanced meridional temperature gradient around 200 hPa (Figure 2d). The most significant increase in the meridional temperature gradient occurs at approximately 25° latitude at tropopause level. Wind speeds in the core of the subtropical jet stream strengthened consistently by approximately 6%, from 53.3 m s^{-1} to 56.9 m s^{-1}. The core of the jet stream also shifts upward by 25 hPa, from 175 hPa in [CNTRL] to 150 hPa in the [SST4] simulation. However, stronger increases exceeding 10 m s^{-1} in zonal wind occur above the jet stream cores due to an increase in the jet stream height, consistent with the increase height of the tropopause (Figure 2g). The upward shift of the jet core is also evident by the decrease in the zonal wind speed below the jet core in the (sub)tropical regions. In addition to the deeper zonal wind distribution, we also find a poleward shift in the jet stream position caused by an expanding tropical atmosphere. The tropical warming pushes

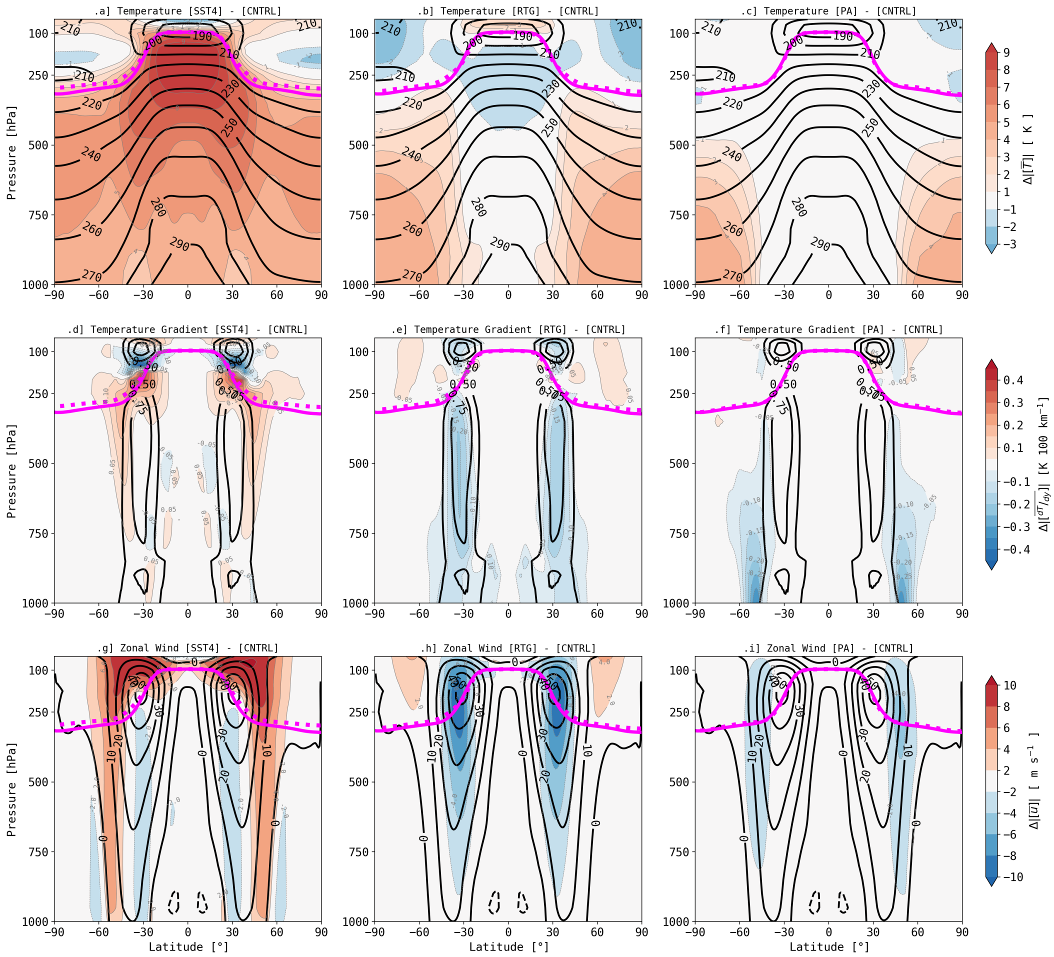

Figure 2. Atmospheric zonal mean climatologies of the ten year simulations. Shading shows the atmospheric responses ($\left|[\overline{\mathrm{EXPERIMENT}}]\right|$-$\left|[\overline{\mathrm{CNTRL}}]\right|$) in temperature $[\overline{T}]$ [K] (a, b, c), meridional temperature gradient $[\frac{\overline{dT}}{dy}]$ [K 100 km^{-1}] (d, e, f) and zonal wind $[\overline{u}]$ [m s^{-1}] (g, h, i) for the [SST4] simulation (column 1), [RTG] simulation (column 2) and [PA] simulation (column 3). Black contour lines represent the [CNTRL] simulation climatologies (labels indicate their values) and magenta contour lines the dynamical tropopause at the 2PVU surface — dashed magenta lines the equivalent in the experiment.

the polar edge of the baroclinic zone poleward as visible in the band of increased temperature gradients and zonal winds in the mid-latitudes (Figures 2d and 2g).

3.2 [RTG] simulation

The [RTG] simulation warms in the lower to mid-troposphere at high latitudes, with a maximum warming of approximately 4.5 K that extended into the mid-latitudes, from where the warming gradually reduces to values of 1 K in the subtropics (Figure 2b). In contrast to the upper tropical warming in the [SST4] simulation, the [RTG] simulation shows cooling in this region. The cooling can be attributed to decreased latent heat release in the rising branch of the Hadley cells (not shown). The tropospheric warming in the [RTG] simulation also results in a deeper troposphere, as indicated by the increased height of the dynamic tropopause poleward of 30° latitude (Figure 2, column 2).

Overall, the effect of lower tropospheric polar warming and upper tropospheric tropical cooling causes a substantial reduction in the tropospheric meridional temperature gradient (Figure 2e). The strongest decrease up to 0.2 K 100 km^{-1} occurs in the mid-latitudes between 25° latitude and 50° latitude in the middle troposphere (Figure 2e). In turn, the reduced meridional temperature gradient impacts the zonal circulation. Zonal winds in the [RTG] simulation decrease substantially throughout the whole troposphere (Figure 2h). Most prominently, the core of the jet stream weakens by approximately 15% to 45.4 m s^{-1}.

3.3 [PA] simulation

Compared to the [RTG] simulation, the warming of the lower to mid-troposphere in the [PA] simulation is more confined to higher latitudes (Figure 2c). The maximum warming of 4 K occurs poleward of 60° latitude in the lower troposphere, while equatorward of 45° latitude, the temperature response was neutral, ranging from -1 K to 1 K.

The most prominent effect of the low-level polar warming is the decrease in the meridional temperature gradient on the poleward edge of the baroclinic zone in the mid-latitudes up to 0.3 K 100 km^{-1} near the surface (Figure 2f). This is the strongest tropospheric meridional temperature-gradient reduction of all experiments and is expected from the prescribed [PA] SST-profile (Figure 1a). The reduced temperature-gradient causes a decrease in zonal wind aloft, poleward of the jet stream core (Figure 2i). Apart from slightly enhanced jet core strength from 1.1 m s^{-1} to 54.4 m s^{-1}, no notable wind speed changes occur in the subtropics of the [PA] simulation.

4 Jet Stream Waviness Response

Next, we study the impact of the altered mean atmospheric state on wave amplitudes, waviness of the jet stream, cut-off segment lengths and the variability within the distributions of these diagnostics (Figure 3).

Our focus is on the extreme tails of the meridional extent and *SI* distributions, assessed through changes in their respective 98th percentiles compared to the [CNTRL] simulation (Figure 3). They correspond to large wave amplitudes and high waviness events that are associated with weather extremes (e.g., Francis & Vavrus, 2015; Cattiaux et al., 2016; Röthlisberger, Pfahl, & Martius, 2016; Coumou et al., 2018), and therefore more sociatally relevant than the mean. To test if the 98th percentiles differ statistically significantly we use the nonparametric quantile test (Johnson et al., 1987). We use the alternative hypothesis 'less' which tests if the probability of the 98th percentile of the experiment simulation has higher values than the [CNTRL] simulation. We also tested the 90th and 95th extreme percentiles (not shown) which gave qualitatively the same results (except for the waviness and cut-off segments diagnostics in the [SST4] simulation). For

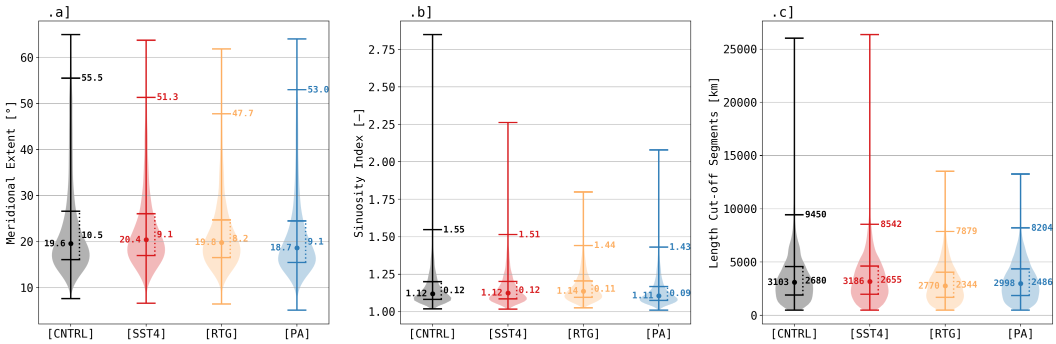

Figure 3. Violin plots for the 6-hourly distributions of (a) the meridional extent [°] of the average $Z500$ in the latitudinal range of the selected $Z500$ isohypses, (b) Sinuosity Index [-] and (c) the length of the cut-off segments of the selected $Z500$ isohypses [km]. Labeled horizontal bars indicate the 98^{th}, 75^{th} and 25^{th} percentile (from top to bottom), and the vertical dotted line represents the interquartile range.

completeness we also analyze the median (50^{th} percentiles) of each diagnostic differs from [CNTRL] using the Brown-Mood test.

Lastly, the variability in the distributions is studied by the interquartile ranges because the distributions are not normally distributed. To evaluate the statistical differences among these interquartile ranges, we employ bootstrapping. Comparisons among the resulting distributions of the computed interquartile ranges (Figure S2) are conducted using a student's t-test.

Now, we first briefly discuss the general changes of the diagnostics supported by statistical tests before we specifically highlight the most substantial changes found in each simulation.

4.1 General changes of the diagnostics

Across all model experiments, and for each diagnostic, the 98^{th} percentile of each distribution show the most prominent changes (Figure 3). We find that the 98^{th} percentiles for each diagnostic is statistically significantly lower in the experiments compared to [CNTRL] as confirmed by the quantile test at the 99% confidence interval.

The shifts in the medians are moderate and vary in sign. Despite the small magnitude of the changes, they are statistically significantly different on the Brown-Mood test at the 99% confidence interval for all diagnostics and simulations except for cut-off segments length in [SST4] and [PA] (Table S1). However, all median changes are relatively minor deviations compared to the natural variability depicted by the interquartile ranges (Figure 3).

Interestingly, the interquartile ranges for each diagnostic in every simulation decreases compared to [CNTRL]. We find that the interquartile ranges for each diagnostic is statistically significantly lower in the experiments compared to [CNTRL] as confirmed by the student's t-test at the 99% confidence interval (Table S1). Hence, this result indicates a consistent reduction in variability of the selected diagnostics across all warming scenarios.

4.2 [SST4] simulation

Comparing the meridional extent distribution between [SST4] and the [CNTRL] (Figure 3a), the 98^{th} percentile decreases from 55.5° to 51.3°. Despite this decrease, the median of the distribution increases slightly from 19.6° to 20.4°. Thus, with uniform warming resulting in upper tropical warming and a strengthened jet stream, there is a robust decrease in the largest wave amplitudes and a slight increase in the median amplitude.

Analyzing the SI distribution (Figure 3b), the 98^{th} percentile decreases from 1.55 in [CNTRL] to 1.51 in [SST4], indicating a decrease in extreme waviness episodes. There are no further alterations in the SI distribution, suggesting only a reduction in high-waviness episodes within [SST4].

Examining the cut-off segments distribution (Figure 3c), the 98^{th} percentile signals a distinct reduction in the length of the longest cut-off segments under uniform warming. Marginal differences are observed in the median, indicating minimal changes in the lengths of cut-off segments of the [SST4] simulation.

4.3 [RTG] simulation

The changes observed in the extreme tail of the meridional extent distribution (Figure 3a) within [RTG] are most pronounced among all experiment simulations. The 98^{th} percentile decreases from 55.5° in [CNTRL] to 47.7° in [RTG]. There is a marginal shift in the median towards higher values. Overall, these changes in the meridional extent of [RTG] suggest that the largest wave amplitudes are smaller in weaker jet streams.

Within the SI distribution (Figure 3b) of [RTG], consistent trends emerge. A notable decrease from 1.55 to 1.44 in the 98^{th} percentile signifies a decrease in extreme waviness episodes. However, a marginal increase in SI of 0.02 in the median is observed. Consequently, weakened jet streams within [RTG] exhibit a distinct decrease in extreme waviness episodes alongside a slight increase in median waviness. This finding suggest that reduced low-level temperature gradients accompanied with weakened jet streams do not promote extreme waviness episodes.

Moreover, prominent reductions observed in the distribution depicting the length of cut-off segments (Figure 3c) within [RTG] indicate a consistent reduction in the length of these segments.

4.4 [PA] simulation

Polar warming stands out as the sole simulation consistently manifesting reductions across all distribution characteristics for each diagnostic (Figure 3). Notably, the 98^{th} percentile of the meridional extent (Figure 3a) decreases from 55.5° in [CNTRL] to 53.0° in [PA]. While the median undergoes a robust yet marginal decrease, collectively, these outcomes suggest a reduction in wave amplitudes under polar warming conditions.

Similar consistent reductions are evident in the SI distributions (Figure 3b). The 98^{th} percentile notably decreases from 1.55 in [CNTRL] to 1.43 in [PA], signifying a substantial decrease in extreme waviness episodes. Additionally, we find a minimal reduction in the median SI of 0.01. These reductions across all distribution characteristics collectively reinforce the evidence supporting decreased jet stream waviness under polar warming conditions.

Once again, in the characteristics related to the length of the cut-off segments (Figure 3c), analogous trends are observed. The 98^{th} percentile and median display reductions in the length of the cut-off segments under polar warming conditions.

5 Discussion and Concluding Remarks

We perform four idealized aquaplanet simulations to study the causality between large-scale spatial warming and jet stream extreme waviness. The results of the experiments contribute to the open question whether the future jet stream is influenced by large-scale spatial warming (e.g., Barnes & Screen, 2015; Shaw et al., 2016; Stendel et al., 2021) and how jet stream waviness would alter (e.g, Vavrus, 2018; Coumou et al., 2018; Cohen et al., 2020). To quantify jet stream waviness on an aquaplanet, we adjust the latitudinal range and the normalization latitude in the computation of the Sinuosity Index by Cattiaux et al. (2016). Using this waviness metric we are able to analyze the length of cut-off segments, which are related to blocking highs and cut-off lows that are associated with mid-latitude weather extremes (Cattiaux et al., 2016).

The idealized aquaplanet simulations generate robust responses in the mean zonal climates of temperature, temperature gradients and zonal wind. Most notably, we find substantial decreases in (large) wave amplitudes, (extreme) jet stream waviness and cut-off segments for almost all simulations in each diagnostic. We enumerate the most prominent results and highlight differences between the simulations:

1. In the [SST4] simulation, uniform warming of 4 K leads to upper tropospheric tropical warming, enhanced meridional temperature gradients, and strengthened jet streams. All three of the circulation diagnostics we consider show a significant decrease in their 98^{th} percentiles and interquartile ranges, thus indicating the extreme waviness events become less wavy and less variable with uniform warming. The median of wave amplitudes, however, show a robust, but marginal increase.
2. Gradual warming from the equator to 5 K at the poles in the [RTG] simulation substantially reduces meridional temperature gradients and weakens jet streams, especially in the subtropical jet core region. All three of the circulation diagnostics we consider depict even more significant decrease in their 98^{th} percentiles in [RTG]. This implies extreme waviness episodes become even less wavy and less variable with meridional temperature gradient reductions. Also in [RTG] the median of wave amplitudes show a marginal increase.
3. Polar warming at high latitudes in the [PA] simulation reduces meridional temperature gradients, primarily in the mid-latitudes and the lower troposphere, that weakens jet streams aloft. The [PA] simulation consistently manifest reduction in the 98^{th} percentiles, medians and interquartile ranges across all three diagnostics. This leads to robust reduced wave amplitudes, decreased waviness episodes and reduced length of cut-off segments in conjunction with decreased variability.

Compared to [CNTRL], the reduced wave amplitudes observed in the [RTG] and [PA] simulations align with findings from Hassanzadeh et al. (2014), who report a decrease in wave amplitude with reduced meridional temperature gradients in dry model simulations. Furthermore, Hassanzadeh et al. (2014) find reduced areas affected by atmospheric blocking in simulations with reduced temperature gradients. While we did not specifically detect blocking, our results indicate consistent findings with shortened cut-off lengths in the reduced temperature gradient simulations [PA] and [RTG]. The only highly idealized study that focuses on jet stream waviness specifically is Schemm and Röthlisberger (2024). They find decreased waviness in 4 K uniform warmed aquaplanet simulations with SSTs representing a summer and winter hemisphere. This is consistent with what we find in [SST4].

The magnitude of all (statistically significant) responses in the median of [SST4], [RTG] and [PA] is small compared to the natural variability of the [CNTRL] simulation. This has previously been noted for reanalysis data (e.g., Barnes, 2013; Screen & Simmonds, 2013; Screen, 2014), comprehensive climate models (e.g., Cattiaux et al., 2016), models with induced sea-ice loss alone (e.g., Blackport & Screen, 2020; Smith et al., 2022) and highly idealized simulations (Hassanzadeh et al., 2014; Schneider et al., 2015).

Additionally, the natural variability reduces as evidenced by the robust decrease in the interquartile range of the distributions of wave amplitude, jet stream waviness and cut-off segments. This suggests that large-scale spatial warming makes the atmospheric circulation less variable. The reduced variability in the experiment simulations is potentially caused by weakened baroclinicity and, hence, the jet stream is less affected by synoptic waves. Schemm and Röthlisberger (2024) find a reduction of synoptic wave amplitude with uniform warming and state that these waves play a more substantial role in shaping the geometric waviness of the jet stream. Indeed, Sinclair and Catto (2023), with identical [SST4] and [PA] simulations, find for uniform warming weakened Eady growth rates and for polar amplification weakened growth rates in the low-to-middle troposphere on the poleward side of the jet, but slight increases in the mid-to-upper troposphere at high latitudes. For our [RTG] simulation we expect even larger reductions in baroclinicity because the natural variability is the lowest in all simulations.

Our results contradict the mechanism proposed by Francis and Vavrus (2012, 2015), that a reduced temperature gradient, consequently, a weaker zonal flow, would lead to amplified and more wavy jet streams, resulting in increased weather extremes. Their hypothesis, however, leans on the linearity assumption of barotropic Rossby wave theory, which may not fully encompass the highly nonlinear behavior observed in the real atmosphere and the aquaplanet's atmosphere. This might be because barotropic Rossby wave theory does not describe nonlinear baroclinic growth of synoptic waves.

Another possible explanation for these results contradicting the mechanism proposed by Francis and Vavrus (2012, 2015), is the use of an aquaplanet where the absence of zonal asymmetries, like orography and land-sea contrasts, eliminates many Rossby wave sources. Moon et al. (2022), have identified thermal forcing, arising from land-sea contrasts, in conjunction with weakened flow, as pivotal factors for generating wavier jet streams. Thus, future idealized experiments could introduce extra complexity by introducing SST perturbations (Brayshaw et al., 2008; Schemm et al., 2022), simple continents (Brayshaw et al., 2009), orography or all these aspects (Brayshaw et al., 2011) in combination with temperature gradient reductions. This approach could provide a more comprehensive understanding of the impact of temperature gradient modifications on jet stream circulation changes and increased weather extremes.

In summary, results from our study demonstrates that large-scale spatial warming on an aquaplanet affects meridional temperature gradients and jet streams. Both strengthened and weakened jet streams show robust decreases in the magnitudes of large wave amplitudes and extreme episodes of jet stream waviness. We suggest that these results are related to reduced baroclinicity in all simulations. Ultimately, we conclude that weaker jet streams do not necessarily become wavier.

6 Open Research

Data archiving is underway. We plan to archive at Zenodo.

Acknowledgments
The authors want to thank ECMWF for making OpenIFS available to the University of Helsinki and Wageningen University. The simulations were carried out on the Dutch national supercomputer Snellius with the support of SURF (`www.surf.nl`, project number NWO-2023.003). VAS was supported by the Research Council of Finland (grant no 338615).

References

Barnes, E. A. (2013). Revisiting the evidence linking arctic amplification to extreme weather in midlatitudes. *Geophysical research letters*, *40*(17), 4734–4739.

Barnes, E. A., & Polvani, L. M. (2015). CMIP5 Projections of Arctic Amplification, of the North American/North Atlantic Circulation, and of Their Relationship. *Journal of Climate*, *28*(13), 5254–5271. (Publisher: American Meteorological Society Section: Journal of Climate) doi: 10.1175/JCLI-D-14-00589.1

Barnes, E. A., & Screen, J. A. (2015). The impact of Arctic warming on the midlatitude jet-stream: Can it? Has it? Will it? *WIREs Climate Change*, *6*(3), 277–286. doi: 10.1002/wcc.337

Blackport, R., & Screen, J. A. (2020). Insignificant effect of arctic amplification on the amplitude of midlatitude atmospheric waves. *Science advances*, *6*(8), eaay2880.

Brayshaw, D. J., Hoskins, B., & Blackburn, M. (2008). The storm-track response to idealized sst perturbations in an aquaplanet gcm. *Journal of the Atmospheric Sciences*, *65*(9), 2842–2860.

Brayshaw, D. J., Hoskins, B., & Blackburn, M. (2009). The basic ingredients of the north atlantic storm track. part i: Land–sea contrast and orography. *Journal of the Atmospheric Sciences*, *66*(9), 2539–2558.

Brayshaw, D. J., Hoskins, B., & Blackburn, M. (2011). The basic ingredients of the north atlantic storm track. part ii: Sea surface temperatures. *Journal of the Atmospheric Sciences*, *68*(8), 1784–1805.

Butler, A. H., Thompson, D. W. J., & Heikes, R. (2010). The Steady-State Atmospheric Circulation Response to Climate Change–like Thermal Forcings in a Simple General Circulation Model. *Journal of Climate*, *23*(13), 3474–3496. doi: 10.1175/2010JCLI3228.1

Cattiaux, J., Peings, Y., Saint-Martin, D., Trou-Kechout, N., & Vavrus, S. J. (2016). Sinuosity of midlatitude atmospheric flow in a warming world. *Geophysical Research Letters*, *43*(15), 8259–8268.

Chen, G., Lu, J., Burrows, D. A., & Leung, L. R. (2015). Local finite-amplitude wave activity as an objective diagnostic of midlatitude extreme weather. *Geophysical Research Letters*, *42*(24), 10–952.

Cohen, J., Zhang, X., Francis, J., Jung, T., Kwok, R., Overland, J., … others (2020). Divergent consensuses on arctic amplification influence on midlatitude severe winter weather. *Nature Climate Change*, *10*(1), 20–29.

Coumou, D., Di Capua, G., Vavrus, S., Wang, L., & Wang, S. (2018). The influence of arctic amplification on mid-latitude summer circulation. *Nature Communications*, *9*(1), 2959.

Di Capua, G., & Coumou, D. (2016). Changes in meandering of the northern hemisphere circulation. *Environmental Research Letters*, *11*(9), 094028.

Doblas-Reyes, F., Sörensson, A., Almazroui, M., Dosio, A., Gutowski, W., Haarsma, R., … Zuo, Z. (2021). Linking global to regional climate change [Book Section]. In V. Masson-Delmotte et al. (Eds.), *Climate change 2021: The physical science basis. contribution of working group i to the sixth assessment report of the intergovernmental panel on climate change* (p. 1363–1512). doi: 10.1017/9781009157896.012

Francis, J. A., & Vavrus, S. J. (2012). Evidence linking arctic amplification to extreme weather in mid-latitudes. *Geophysical research letters*, *39*(6).

Francis, J. A., & Vavrus, S. J. (2015). Evidence for a wavier jet stream in response to rapid Arctic warming. *Environmental Research Letters*, *10*(1), 014005. doi: 10.1088/1748-9326/10/1/014005

Gulev, S., Thorne, P., Ahn, J., Dentener, F., Domingues, C., Gerland, S., … Vose, R. (2021). Changing state of the climate system [Book Section]. In V. Masson-Delmotte et al. (Eds.), *Climate change 2021: The physical science basis. contribution of working group i to the sixth assessment re-*

port of the intergovernmental panel on climate change (p. 287–422). doi: 10.1017/9781009157896.004

Hassanzadeh, P., Kuang, Z., & Farrell, B. F. (2014). Responses of midlatitude blocks and wave amplitude to changes in the meridional temperature gradient in an idealized dry gcm. *Geophysical Research Letters*, *41*(14), 5223–5232.

Hersbach, H., Bell, B., Berrisford, P., Hirahara, S., Horányi, A., Muñoz-Sabater, J., ... others (2020). The era5 global reanalysis. *Quarterly Journal of the Royal Meteorological Society*, *146*(730), 1999–2049.

IPCC. (2021). *Climate change 2021: The physical science basis. contribution of working group i to the sixth assessment report of the intergovernmental panel on climate change* [Book]. doi: 10.1017/9781009157896

Johnson, R. A., Verrill, S., & Moore, D. H. (1987). Two-sample rank tests for detecting changes that occur in a small proportion of the treated population. *Biometrics*, 641–655.

Lee, J.-Y., Marotzke, J., Bala, G., Cao, L., Corti, S., Dunne, J., ... Zhou, T. (2021). Future global climate: Scenario-based projections and near-term information [Book Section]. In V. Masson-Delmotte et al. (Eds.), *Climate change 2021: The physical science basis. contribution of working group i to the sixth assessment report of the intergovernmental panel on climate change* (p. 553–672). doi: 10.1017/9781009157896.006

Martin, J. E. (2021). Recent Trends in the Waviness of the Northern Hemisphere Wintertime Polar and Subtropical Jets. *Journal of Geophysical Research: Atmospheres*, *126*(9), e2020JD033668. doi: 10.1029/2020JD033668

Moon, W., Kim, B.-M., Yang, G.-H., & Wettlaufer, J. S. (2022). Wavier jet streams driven by zonally asymmetric surface thermal forcing. *Proceedings of the National Academy of Sciences*, *119*(38), e2200890119.

Mori, M., Kosaka, Y., Watanabe, M., Nakamura, H., & Kimoto, M. (2019). A reconciled estimate of the influence of Arctic sea-ice loss on recent Eurasian cooling. *Nature Climate Change*, *9*(2), 123–129. doi: 10.1038/s41558-018-0379-3

Neale, R. B., & Hoskins, B. J. (2000). A standard test for agcms including their physical parametrizations: I: The proposal. *Atmospheric Science Letters*, *1*(2), 101–107.

Ogawa, F., Keenlyside, N., Gao, Y., Koenigk, T., Yang, S., Suo, L., ... Semenov, V. (2018). Evaluating Impacts of Recent Arctic Sea Ice Loss on the Northern Hemisphere Winter Climate Change. *Geophysical Research Letters*, *45*(7), 3255–3263. doi: 10.1002/2017GL076502

Peings, Y., Cattiaux, J., Vavrus, S., & Magnusdottir, G. (2017). Late Twenty-First-Century Changes in the Midlatitude Atmospheric Circulation in the CESM Large Ensemble. *Journal of Climate*, *30*(15), 5943–5960. doi: 10.1175/JCLI-D-16-0340.1

Röthlisberger, M., Martius, O., & Wernli, H. (2016). An algorithm for identifying the initiation of synoptic-scale Rossby waves on potential vorticity waveguides. *Quarterly Journal of the Royal Meteorological Society*, *142*(695), 889–900. doi: 10.1002/qj.2690

Röthlisberger, M., Pfahl, S., & Martius, O. (2016). Regional-scale jet waviness modulates the occurrence of midlatitude weather extremes. *Geophysical Research Letters*, *43*(20), 10,989–10,997. doi: 10.1002/2016GL070944

Schemm, S., Papritz, L., & Rivière, G. (2022). Storm track response to uniform global warming downstream of an idealized sea surface temperature front. *Weather and Climate Dynamics*, *3*(2), 601–623.

Schemm, S., & Röthlisberger, M. (2024). Aquaplanet simulations with winter and summer hemispheres: model setup and circulation response to warming. *Weather and Climate Dynamics*, *5*(1), 43–63. doi: 10.5194/wcd-5-43-2024

Schneider, T., Bischoff, T., & Płotka, H. (2015). Physics of changes in synoptic midlatitude temperature variability. *Journal of Climate*, *28*(6), 2312–2331.

Screen, J. A. (2014). Arctic amplification decreases temperature variance in northern mid-to high-latitudes. *Nature Climate Change*, *4*(7), 577–582.
Screen, J. A., Deser, C., Smith, D. M., Zhang, X., Blackport, R., Kushner, P. J., ... Sun, L. (2018). Consistency and discrepancy in the atmospheric response to arctic sea-ice loss across climate models. *Nature Geoscience*, *11*(3), 155–163.
Screen, J. A., & Simmonds, I. (2013). Exploring links between Arctic amplification and mid-latitude weather. *Geophysical Research Letters*, *40*(5), 959–964. doi: 10.1002/grl.50174
Shaw, T. A., Baldwin, M., Barnes, E. A., Caballero, R., Garfinkel, C. I., Hwang, Y.-T., ... Voigt, A. (2016). Storm track processes and the opposing influences of climate change. *Nature Geoscience*, *9*(9), 656–664. doi: 10.1038/ngeo2783
Sinclair, V. A., & Catto, J. L. (2023). The relationship between extra-tropical cyclone intensity and precipitation in idealised current and future climates. *Weather and Climate Dynamics*, *4*(3), 567–589. doi: 10.5194/wcd-4-567-2023
Sinclair, V. A., Rantanen, M., Haapanala, P., Räisänen, J., & Järvinen, H. (2020). The characteristics and structure of extra-tropical cyclones in a warmer climate. *Weather and Climate Dynamics*, *1*(1), 1–25. doi: 10.5194/wcd-1-1-2020
Smith, D. M., Eade, R., Andrews, M., Ayres, H., Clark, A., Chripko, S., ... others (2022). Robust but weak winter atmospheric circulation response to future arctic sea ice loss. *Nature communications*, *13*(1), 727.
Smith, D. M., Screen, J. A., Deser, C., Cohen, J., Fyfe, J. C., García-Serrano, J., ... others (2019). The polar amplification model intercomparison project (pamip) contribution to cmip6: investigating the causes and consequences of polar amplification. *Geoscientific Model Development*, *12*(3), 1139–1164.
Stendel, M., Francis, J., White, R., Williams, P. D., & Woollings, T. (2021). Chapter 15 - The jet stream and climate change. In T. M. Letcher (Ed.), *Climate Change (Third Edition)* (pp. 327–357). doi: 10.1016/B978-0-12-821575-3.00015-3
Vallis, G. K. (2020). The Trouble with Water: Condensation, Circulation and Climate. *The European Physical Journal Plus*, *135*(6), 478. doi: 10.1140/epjp/s13360-020-00493-7
Vavrus, S. J. (2018). The influence of arctic amplification on mid-latitude weather and climate. *Current Climate Change Reports*, *4*, 238–249.
Woollings, T., Barriopedro, D., Methven, J., Son, S.-W., Martius, O., Harvey, B., ... Seneviratne, S. (2018). Blocking and its response to climate change. *Current climate change reports*, *4*, 287–300.
Woollings, T., Drouard, M., O'Reilly, C. H., Sexton, D. M., & McSweeney, C. (2023). Trends in the atmospheric jet streams are emerging in observations and could be linked to tropical warming. *Communications Earth & Environment*, *4*(1), 125.

Supporting Information for "The Influence of Large-Scale Spatial Warming on Jet Stream Extreme Waviness on an Aquaplanet"

T. J. Batelaan[1], C. Weijenborg[1], G.J. Steeneveld[1], C. C. van Heerwaarden[1],

V. A. Sinclair[2]

[1]Meteorology and Air Quality Section, Environmental Sciences Group, Wageningen University, P.O. Box 47, 6700 AA Wageningen, The Netherlands

[2]Institute for Atmospheric and Earth System Research/Physics, Faculty of Science, University of Helsinki, P.O. Box 64, 00014, Helsinki, Finland

Contents of this file

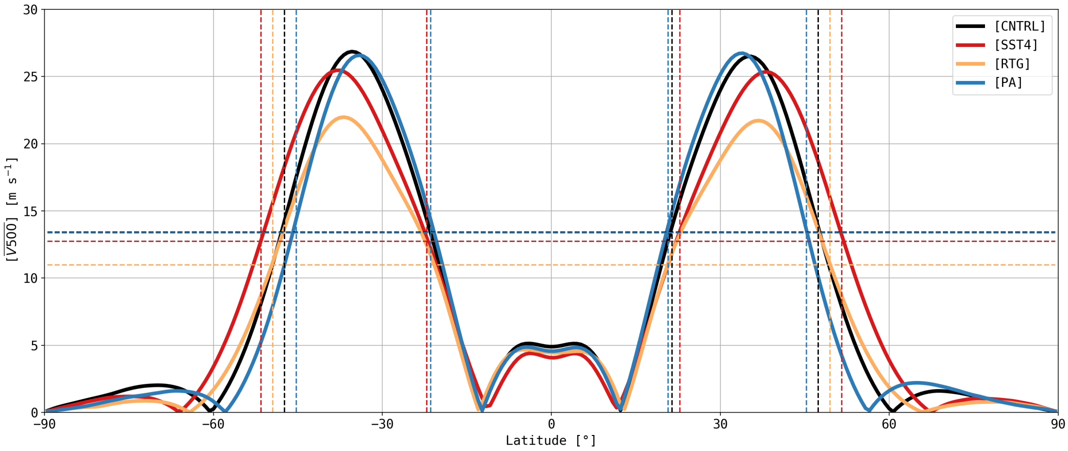

Figure S1. Time mean zonal mean of the magnitude of the 500-hPa horizontal wind vector $[\overline{V_{500}}]$ [m s^{-1}] for each simulation. Horizontal dashed lines show the half of the maximum $[\overline{V_{500}}]$ thresholds and vertical dashed lines the latitude range where this thresholds was exceeded. These latitude ranges are used to estimate the modified Sinuosity Index.

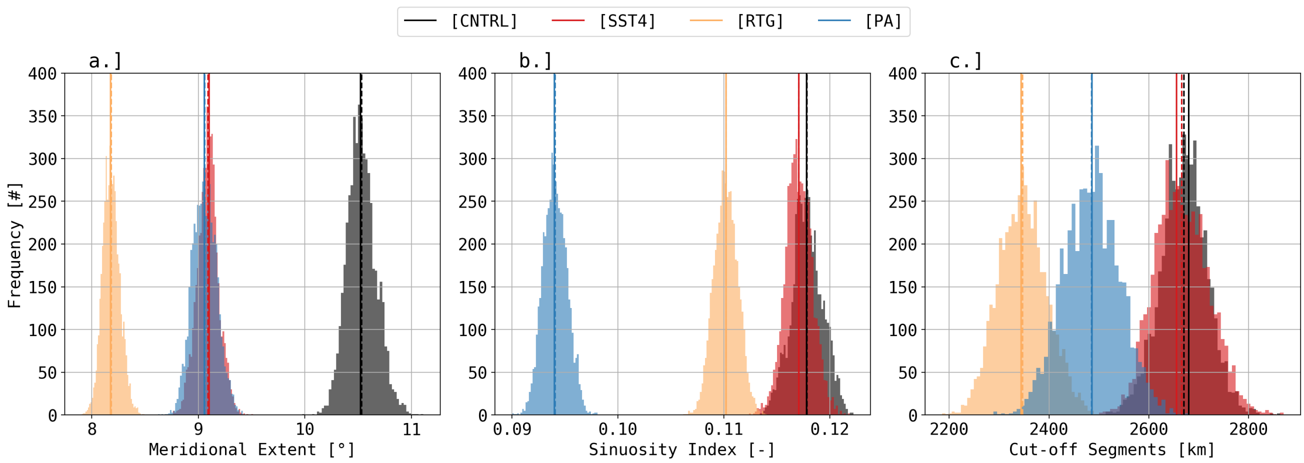

Figure S2. Distributions of the interquartile ranges of (a) meridional extent [°], (b) Sinuosity Index [-] and (c) cut-off segments length [km] for each simulation obtained from bootstrapping. In this process, we iteratively resample the data 5000 times for each simulation and diagnostic and maintain the same sample size of the original datasets. Subsequently, interquartile ranges are computed for each of these 5000 resamples. The dashed vertical lines are the means of the distributions and the continuous vertical lines are the interquartile ranges from the original datasets (Figure 3).

Table S1. P-values from quantile test, Brown-Mood test and student's t-test that tests 6-hourly distributions ($N = 2 \times (10 \times 365 \times 4) + 2 \times (8) = 29216$, because we simulate ten years, including two leap years, of two identical hemispheres). For the quantile test on the 98^{th} the alternative hypothesis 'less' is chosen. Hence, it tests if the probability of the 98^{th} percentile of the experiment simulation has higher values than the [CNTRL] simulation. A Brown-Mood test is identical to a two-sided quantile test at the 50^{th} percentile. P-values of student's t-test that tests interquartile range distributions obtained by bootstrapping (N=5000). P-values lower than p=0.01 are bold and there the simulation differ from the [CNTRL] simulation in a statistically significant manner on the 99% confidence interval. P-values smaller than p=0.0005 — and larger than zero — are shown with **p<0.000**.

Quantile test (98^{th} percentile):

[CNTRL] vs.	Meridional Extent	Sinuosity Index	Length Cut-off Segments
[SST4]	**p<0.000**	**p=0.001**	**p<0.000**
[RTG]	**p<0.000**	**p<0.000**	**p<0.000**
[PA]	**p<0.000**	**p<0.000**	**p=0.004**

Brown-Mood test (50^{th} percentile):

[CNTRL] vs.	Meridional Extent	Sinuosity Index	Length Cut-off Segments
[SST4]	**p<0.000**	**p<0.000**	p=0.054
[RTG]	**p<0.000**	**p<0.000**	**p<0.000**
[PA]	**p<0.000**	**p<0.000**	p=0.023

Student's t-test:

[CNTRL] vs.	Meridional Extent	Sinuosity Index	Length Cut-off Segments
[SST4]	**p<0.000**	**p<0.000**	**p<0.000**
[RTG]	**p<0.000**	**p<0.000**	**p<0.000**
[PA]	**p<0.000**	**p<0.000**	**p<0.000**